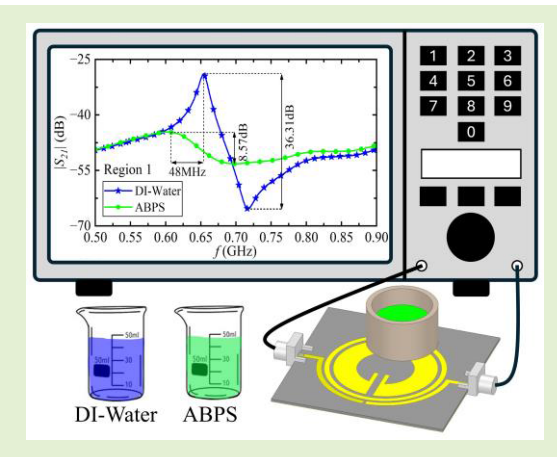


Microwave Glucose Sensing Using Double Circular Split Ring Resonators for Improved Sensitivity: The Role of Artificial Blood Plasma and Deionized Water

Mateus I. O. Souza[®], Natália M. Santos[®], Júlio C. P. Alarcon[®], Laudemir C. Varanda[®], Vinicius M. Pepino[®], and Ben-Hur V. Borges[®]

Abstract—In 2021, approximately 537 million people were diagnosed with diabetes mellitus. With rates expected to rise, health expenditures are projected to reach one trillion USD by 2030. Thus, measuring glucose levels is essential for rationalizing the costs of public health systems. In this context, this article presents two major contributions. First, it demonstrates that using deionized water (DI-water) as a reference for glucose sensing is not a reliable approach for representing human blood plasma (BP), as it lacks ions and suppresses essential effects such as losses. As an alternative, we investigate the use of an artificial BP solution (ABPS) that closely resembles real human BP. Characterized over a range from 500 MHz to 10 GHz, ABPS shows marginal differences in real permittivity but significant differences in imaginary permittivity compared to DI-water. The second contribution is the design of a highly sensitive microwave (MW) sensor based on double concentric circular



split ring resonator (DCCSRR) on a 49 \times 45 mm ROGERS 5880 TM substrate. This sensor can differentiate glucose concentrations from 0 to 400 mg/dL, exceeding the relevant range for diabetic individuals (50–300 mg/dL). The DCCSRR operates at 2.48 GHz and can detect minimal concentration variations of 25 mg/dL in low concentrations, representing a significant advancement in the field. Different from most sensitive approaches available to date, this structure operates in a nonlicensed band and a fully passive form, offering flexibility for implementation and low cost. These characteristics position it as a state-of-the-art solution in MW glucose sensors.

Index Terms—Artificial blood plasma (BP), dielectric characterization, glucose sensing, microwave (MW) sensor.

Received 14 November 2024; accepted 5 December 2024. Date of publication 18 December 2024; date of current version 31 January 2025. This work was supported in part by the Coordination for the Improvement of Higher Education Personnel (CAPES) under Grant 001, in part by the National Council of Scientific and Technological Development (CNPq) under Grant 304208/2021-3, and in part by São Paulo Research Foundation (FAPESP) under Grant 2013/07276-1 and Grant 2020/06501-5. The associate editor coordinating the review of this article and approving it for publication was Prof. Ibraheem Al-Naib. (Corresponding author: Ben-Hur V. Borges.)

Mateus I. O. Souza, Júlio C. P. Alarcon, Vinicius M. Pepino, and Ben-Hur V. Borges are with the Department of Electrical Engineering and Computing, São Carlos School of Engineering, University of São Paulo, Campus São Carlos, São Carlos, São Paulo 13566-590, Brazil (e-mail: mateusafk@usp.br; julio.alarcon@usp.br; vinicius.pepino@usp.br; benhur@sc.usp.br).

Natália M. Santos and Laudemir C. Varanda are with the Department of Physical-Chemistry, Institute of Chemistry of São Carlos, University of São Paulo, Campus São Carlos, São Carlos, São Paulo 13566-590, Brazil (e-mail: nmsantos@usp.br; lvaranda@iqsc.usp.br).

This article has supplementary downloadable material available at https://doi.org/10.1109/JSEN.2024.3516571, provided by the authors. Digital Object Identifier 10.1109/JSEN.2024.3516571

I. INTRODUCTION

CCORDING to the International Diabetes Federation (IDF), in 2021, 537 million people were diagnosed with diabetes mellitus. This is a troubling scenario, as diabetes has no cure, and incidence rates are expected to rise, affecting children, adolescents, and adults alike. Predictions indicate that global health expenditures will reach one trillion USD by 2030, increasing concerns among global authorities [1].

Diabetes manifests in two forms: type-1 and type-2. In type-1 diabetes, the immune system destroys the beta cells responsible for insulin production, making it impossible to regulate glycemia, which controls glucose levels in the blood-stream. Although less prevalent, type-1 diabetes remains a significant issue. In contrast, type-2 diabetes is more common, accounting for 96% of cases in 2021 [2]. In type-2 diabetes, the beta cells produce insulin, but not effectively, necessitating adjustments to hormonal levels.

Administering the correct insulin dosage typically involves measuring glycemia levels. The traditional method requires pricking the fingertip with a blade to collect a blood sample for use in an electrochemical sensor. This sensor reads the current amplitude produced by the reaction between the sample and the oxidase enzyme (GOx) on a strip. While effective, this method is uncomfortable, requiring multiple daily measurements, which can lead to complications such as irritations or infections. Moreover, the relatively high cost of glucometers and strips makes it unaffordable for many. In addition, electrochemical devices have a limited lifespan, necessitating replacement over time. Of course, the best alternative is a noninvasive approach [3], [4], [5] due to its potential to improve patient comfort, eliminate infection risks, and simplify continuous monitoring of biomedical parameters. However, current technology still faces significant challenges in terms of sensitivity, accuracy, and cost, limiting its widespread application. As will be described later in this section, most of the references listed below (encompassing both invasive and noninvasive approaches) share the same issue when it comes to the reference media they use, which is deionized water (DI-water).

Currently, there is no commercially available technology that offers both noninvasive operation and affordability. However, some emerging options show promise in meeting these conditions. One such example is microstrip line (ML) sensors, operating in the microwave (MW) band, but at low frequencies, offering sufficient sensitivity and low-cost. While in the past, these sensors were unable to measure glucose concentrations comparable to bloodstream levels [6], recent advances have made this capability a reality [7], [8], [9], [10], [11], [12], [13], [14], [15]. Moreover, their low manufacturing costs and seamless integration with electronic systems make ML sensors a good choice for exploration [16]. With increasing sensitivity over time and their cost-effectiveness, there is a strong belief that ML sensors could soon replace current invasive methods [17], [18]. Certainly, ML sensors are not the only category of sensors with the potential to detect glucose variations in the human body. To provide a more comprehensive comparison and explore other viable alternatives, we have added an additional topic to the Supplementary Material, discussing other sensor technologies.

It is well-known that MLs encompass a diverse array of applications, including filters [19], [20], antennas [21], [22], transmission lines [23], metamaterials [24], [25], and resonators [26], [27]. Among these applications, resonators stand out for their extensive use in sensing due to their capacity to generate strong electromagnetic fields at specific frequencies. These fields, easily detected using a vector network analyzer (VNA), show a distinct resonance signature. When considering biomedical applications, resonators are an innovative approach for sensing various biological samples, including blood plasma (BP). By placing a real BP sample near the resonator, the electromagnetic fields interact with the material, inducing changes in resonance parameters. These changes, ranging from shifts in transmission (ΔS_{21}) and reflection amplitudes (ΔS_{11}), to alterations in the resonant

frequency (Δf_r) and quality factor (ΔQ) , provide valuable insights into the composition and properties of the sample.

In [7], [8], [9], and [15] the proposed sensors operated by measuring the glucose concentration based on changes in $|S_{21}|$. In [7], a resonator designed on a ceramic substrate was assessed based on temperature changes in the sample. A coefficient was determined to correct the measured values, thereby reducing error. Jang et al. [8], [15] utilized two complementary split-ring resonators (CSRRs) coupled with other active elements, forming an interferometric system for thermal noise reduction. This strategy effectively stabilized and improved the sensitivity of the CSRRs. In [9], the measured samples were positioned beneath the copper trail of a transmission line, where the electric fields are stronger. In this arrangement, the samples interacted more strongly with the sensor's fields, thus increasing sensitivity.

Zidane et al. [10] presented a set of split-ring resonators (SRRs), in which the measured parameter with the glucose variation was $|S_{11}|$. Despite good resolution (50 mg/dL), the device utilizes active components, thereby increasing fabrication costs. Alternatively, there are sensors that assess glucose concentration through frequency shifting (Δf_r) [11], [12]. In [11], an antenna achieved a resolution of 100 mg/dL with significant frequency shifting, but its elevated operating frequency range increases the technology costs. In [9], a structure exhibited extremely high-frequency shifting. However, no tests were presented to demonstrate how concentration curves behave when measurements are repeated. Yi and Wang [13] and Wang et al. [14] employed multiple parameters to map glucose concentrations. In [13], a defective-ground-structure coplanar waveguide was proposed as sensor, with Δf_r and ΔS_{11} serving as the reference parameters. In [14], a new error correction methodology based on the Δf_r and $|S_{21}|$ readings from adjacent concentrations was introduced, improving the sensor's accuracy.

A new category of MW sensors has emerged, designed to measure glucose levels noninvasively by simply positioning the fingertip over the sensing area. To achieve this, researchers are integrating active MW sensors with machine learning techniques. Kazemi and Musilek [28] developed an active resonator combined with a cycle generative adversarial network (CycleGAN) to infer glucose levels noninvasively from interstitial fluid. Measurements were evaluated in both passive and active modes. In [29], an SRR coupled to a patch was used with a long short-term memory (LSTM) algorithm to predict glucose concentration events 30 and 60 min in advance, using interstitial fluid as the target sample. The results showed strong agreement with readings from a commercial glucometer used as a reference. Although these approaches are relatively new, they represent significant progress toward fully noninvasive devices operating in the MW band.

Note that the previous structures can be classified as either passive [7], [8], [9], [10], [11], [12], [13] or active [14], [15], [28], [29] sensors. Passive sensors are generally preferred due to their self-sufficiency, requiring no additional components for operation, which reduces fabrication costs.

However, active sensors typically exhibit superior performance compared to passive ones.

As previously mentioned, most of the previous approaches have relied on DI-water with added glucose as test samples. While this is a fair approximation, considering that BP is composed of 92% water [30], it does not properly represent real scenarios, as it neglects several ion concentrations present in human plasma. Therefore, we investigate a new reference solution capable of reliably mimicking a real human blood sample. This new reference is called artificial BP solution (ABPS), synthesized in the laboratory as described in [31], considering conventional simulated body fluid (c-SBF) as reference. In addition, we characterize the electromagnetic properties of ABPS-glucose solutions in a frequency band ranging from 500 MHz to 10 GHz by adding pure glucose to form five different concentrations (0, 100, 200, 300, and 400 mg/dL), aiming to fully represent the glycemic variations observed in human blood.

Furthermore, upon closer examination, it becomes evident that the passive devices investigated thus far have a limit to measure variations of 50 mg/dL in glucose concentration, when repeated measurements are assumed. To address the gap between current limitations and ideal performance, we propose a novel MW sensor consisting of a double concentric circular SRR (DCCSRR). The sensor improves the variation to 25 mg/dL in low concentration levels (0–50 mg/dL) and shows the capability to capture 50 mg/dL of variation for the proposed concentrations (0–400 mg/dL), encompassing the relevant range for glucose monitoring in diabetes patients (50–300 mg/dL) [32]. The DCCSRR can achieve this benchmark passively, demonstrating superior performance even when compared to active sensors.

This article is organized as follows. Section II outlines the method employed for the electromagnetic characterization of ABPS and compares its characteristics with those of conventional DI-water samples. Section III presents the design, fabrication, and testing of a new sensor, utilizing DI-water and ABPS as reference samples and examining their effects on the sensor performance. Section IV evaluates the sensor performance and compares it with recent studies. Finally, Section V provides the conclusion and final remarks.

II. ELECTROMAGNETIC CHARACTERIZATION OF THE ARTIFICIAL BP

In general, DI-water is commonly used as a reference to represent BP in sensor platforms. As the name suggests, DI-water lacks ions, which are present in real BP. Therefore, using DI-water as a reference for BP representation fails to account for the ion effect. In contrast, ABPS, particularly the c-SBF assessed in [31], accurately represents this effect, making it a more accurate representation of BP than DI-water. Fig. 1 shows the most relevant ions found in BP, with the blue bars representing their concentrations and the orange bars representing the concentrations in ABPS. ABPS closely mimics a real BP sample, with only minor differences in ion concentrations, such as Cl⁻ and HCO₃⁻, being, therefore, a reliable reference for BP.

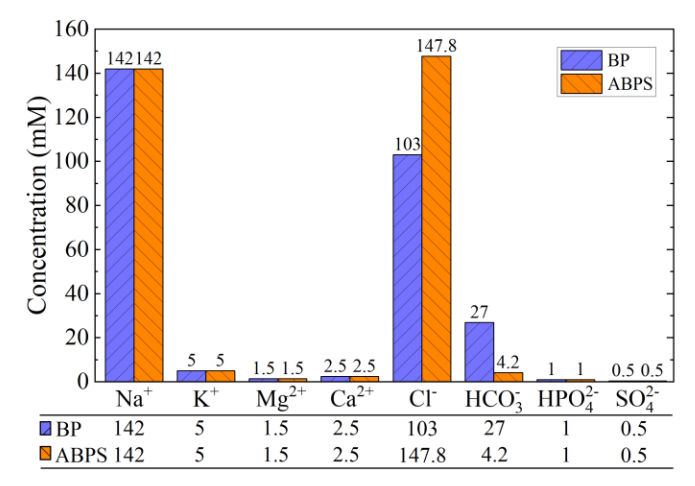


Fig. 1. Comparison between the ion concentrations found in BP and those present in the ABPS, showing minor differences for CI^- and HCO_2^- .

To understand the electromagnetic response of ABPS, we must first extract its frequency dependent, complex relative permittivity $\varepsilon_r(f)$. The complex relative permittivity of a material is defined as follows:

$$\varepsilon_r(f) = \varepsilon'(f) j \varepsilon''(f)$$
 (1)

where $\varepsilon'(f)$ represents the real part of the dielectric constant, $\varepsilon''(f)$ the imaginary part (associated with the dielectric loss), and f is the frequency.

One method for experimentally determining $\varepsilon_r(f)$ is to use an open-ended coaxial probe with a network or impedance analyzer. Such probes are available in commercial kits; however, these kits can be quite costly. Alternatively, methodologies described in the literature, such as the approach outlined in [33], yield comparable results. This alternative involves the fabrication of a probe, as described in [34]. The principal component of this probe is an open-ended coaxial cable, with polytetrafluoroethylene (PTFE) as the dielectric material, attached to a brass housing for rigidness. The probe is connected to a VNA (R&S ZVA-40), which is calibrated within the desired bandwidth. Subsequently, the reflection coefficient (S_{11}) is measured under three conditions: open circuit, short circuit, and submersion in a reference liquid (DI-water). The probe is then immersed in the target sample, and S_{11} is measured again. Using the acquired data and the equations from [33], the complex permittivity of the target sample is determined.

The experimental setup for the characterization of ABPS is shown in Fig. 2. The probe is connected to the VNA cable, affixed to a support, and immersed in pure water. A beaker is used to contain the liquid, while a moving platform facilitates the probe's immersion, ensuring its stable position. To prevent interference from the metallic platform, a foam block is used as a spacer. The inset shows the probe in detail and its dimensions.

To reproduce glycemia variation, glucose powder (99.9% purity, NOX brand) was proportionally added to the ABPS sample, aiming to achieve the following concentrations: 0, 100, 200, 300, and 400 mg/dL. These concentrations were selected

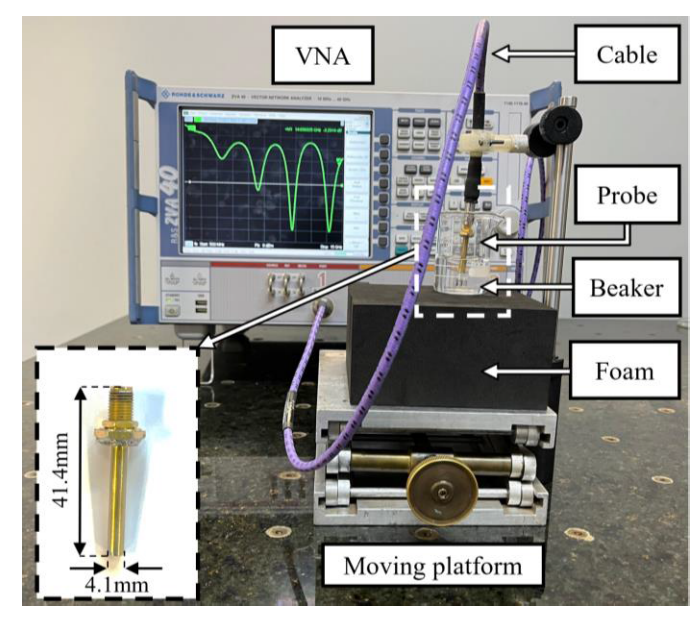


Fig. 2. Setup used for ABPS characterization, where the probe appears affixed to a support and immersed in pure water as the reference liquid. The VNA screen shows the S_{11} response for DI-water, from 500 MHz to 10 GHz, at 25 °C \pm 0.5 °C.

as they encompass the relevant range for glucose monitoring in diabetes patients [32]. S-parameter data were collected from the VNA across a frequency range of 500 MHz–10 GHz, with the room temperature maintained at 25 °C \pm 0.5 °C.

Following data acquisition, it is essential to apply a mathematical model to represent the complex permittivity of the samples. The Cole–Cole model, known for its accurate representation of biological media [31], is particularly relevant for characterizing the ABPS. The Cole–Cole model is defined as follows:

$$\varepsilon_r^*(f) = \varepsilon_\infty + \sum_n \frac{\Delta \varepsilon_n}{1 + (j2\pi f \tau_n)^{1-\alpha_n}} + \frac{\sigma_i}{j2\pi f \varepsilon_0}$$
 (2)

where ε_{∞} refers to the limit of permittivity as angular frequency nears infinity, n is the order of the Cole–Cole model, $\Delta \varepsilon_n$ is the magnitude of dispersion, ε_o is the permittivity of the vacuum, τ_n is the relaxation time constant, α_n is the dispersion-broadening parameters, and σ_i is the static ionic conductivity.

The experimental data were used to fit models for each concentration, with parameters accurately estimated to reproduce the experimental curves with high fidelity. The mean *R*-squared value for the fit curves was 0.9978, indicating excellent agreement between the experimental data and the model. The experimental and fit curves for all concentrations, including the estimated parameters, are provided in the Supplementary Material, specifically in Fig. S1 and Table S1.

Fig. 3(a) illustrates the real permittivity of ABPS for two cases: with no glucose concentration ($\varepsilon'_{ABPS,000}$) and with 400 mg/dL of glucose ($\varepsilon'_{ABPS,400}$). The dashed lines show that these curves are closely aligned, indicating that the changes in ABPS permittivity are minimal for small variations. The blue solid line represents the real permittivity of DI-water ($\varepsilon'_{DI-water}$), as obtained from [35], and contrasts with $\varepsilon'_{ABPS,000}$ as the frequency increases. Fig. 3(b) maintains

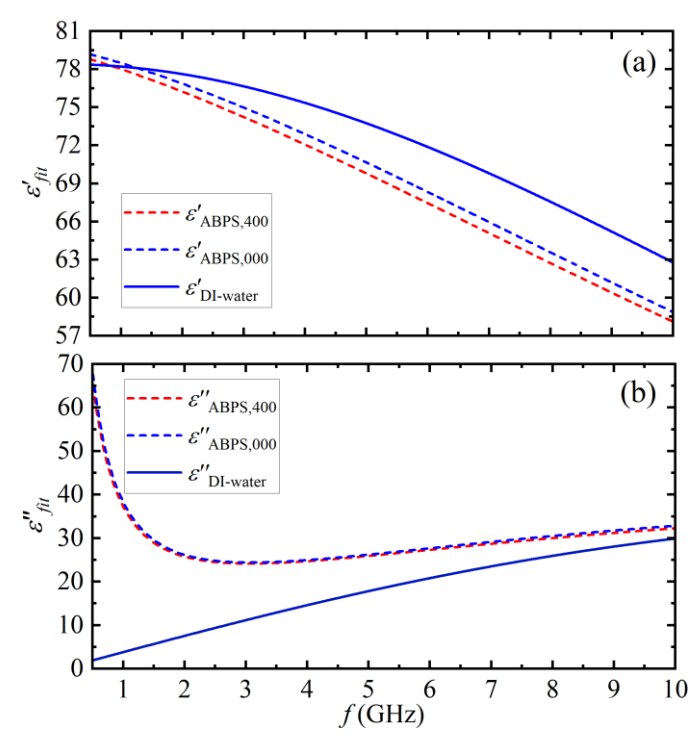


Fig. 3. Comparison of the complex permittivity curves for DI-water (solid lines) and ABPS (dashed lines) when no glucose level is present (blue dashed lines) and when 400 mg/dL is considered (red dashed lines). The models were obtained using the Cole—Cole model, with (a) real part and (b) imaginary part.

the same notations for the liquids, but for the imaginary part of the permittivity. It is evident that ABPS exhibits significantly high losses across the entire frequency range, with even higher losses from 500 MHz to 2 GHz, suggesting an unfavorable region for sensing applications. Conversely, the frequency range from 2 to 3 GHz is the lowest loss region, indicating a more favorable region when using ABPS. In addition, a comparison of the pure solutions, $\varepsilon''_{ABPS,000}$ and $\varepsilon''_{DI-water}$, reveals substantial differences, particularly at lower frequencies, indicating that ABPS and DI-water samples will exhibit significantly different responses when subjected to testing with sensors at these frequencies. For frequencies above 3 GHz, the curves tend to converge to similar values.

To assess the similarity between the real and imaginary parts of the complex permittivity for DI-water and ABPS, Pearson's correlation coefficient (ρ) is employed. The possible values range from -1 to +1, where a negative value indicates a negative correlation, zero indicates no correlation, and +1 indicates a positive correlation. The coefficients are used to compare $\varepsilon'_{\text{DI-water}}/\varepsilon'_{\text{ABPS,000}}$ and $\varepsilon''_{\text{DI-water}}/\varepsilon'_{\text{ABPS,000}}$, as described by the following equation:

 $\rho(X_{\text{DI-W}}X_{\text{ABPS}})$

$$= \frac{1}{N-1} \sum_{i}^{N} \left(\frac{X_{\text{DI-W}_{i}} - \mu_{\text{DI-W}}}{\sigma_{\text{DI-W}}} \right) \left(\frac{X_{\text{ABPS}_{i}} - \mu_{\text{ABPS}}}{\sigma_{\text{ABPS}}} \right). (3)$$

Let $X_{\text{DI-W}_i}$ represent the data corresponding to DI-water, $\mu_{\text{DI-W}}$ denote its mean, and $\sigma_{\text{DI-W}}$ its standard deviation. Similarly, X_{ABPS_i} , μ_{ABPS} and σ_{ABPS} represent the corresponding values for ABPS. The calculated coefficients are

99.25% for the real part of permittivity and -13.43% for the imaginary part. As anticipated, ABPS and DI-water exhibit similar electromagnetic characteristics for the real part but differ significantly in terms of losses, a discrepancy that arises because of the ions present in ABPS, thereby confirming the initial hypothesis. Consequently, when ABPS is used as a sample reference for blood glucose sensing, it is expected to provide a higher level of accuracy compared to DI-water.

Having discussed the electromagnetic properties and distinct characteristics of these two media, the next step is to propose a new sensor and evaluate it using the corresponding samples. Details of this process are presented in Section III.

III. SENSOR DESIGN AND FABRICATION

SRRs consist of a pair of concentric, open rings with gaps on opposite sides. Originally, these structures were developed to create metamaterials with negative refractive index [36], [37], [38]. Over time, SRRs have enabled numerous applications, including oscillators [39], filters [40], antennas [41], and sensors [17], [18], [19], [20], [21], [22]. The proposed sensor is a DCCSRR, which is derived from the classic SRR geometry. Two critical design requirements were established for the DCCSRR: 1) it must exhibit a bandpass response and 2) it must operate within the industrial, scientific, and medical (ISM) band at 2.4–2.48 GHz [48].

The bandpass response is essential for maintaining high amplitudes at resonance peaks, which are typically used as reference points for sensing. Structures with a stopband response tend to degrade the signal-to-noise ratio (SNR) at resonance valleys, compromising the detection accuracy. To illustrate, a variation of 50 mg/dL in glucose concentration in water at 2.5 GHz corresponds to a change in the dielectric constant of $\Delta \varepsilon_r = 0.026$ [49]. Detecting this perturbation passively via resonance shift is challenging, so measuring it through resonance amplitude variation is preferred; therefore, a high SNR is necessary to precisely detect small amplitude variations. In this sense, a bandpass response is more suitable for such applications. The ISM band offers several advantages for commercial sensors, including exemption from licensing requirements, ease of integration with other components, and interoperability, all of which contribute to a lower-cost device in the commercial phase.

Following these design criteria, simulations were conducted using the high-frequency structure simulator (HFSS) software [50], resulting in the final DCCSRR design shown in Fig. 4(a). The DCCSRR is designed on a 0.787-mm-thick ROGERS 5880¹ substrate ($\varepsilon_r = 2.2 - j0.002$). The yellow regions represent the copper areas, while the gray areas depict the substrate. The associated dimensions are listed in Table I. Fig. 4(b) and (c) illustrates the electric field distributions over the DCCSRR at $f_1 = 985$ MHz and $f_2 = 3$ GHz, respectively. The frequency response for magnitude transmission of the DCCSRR, ranging from 0.5 to 3.5 GHz, is shown in Fig. 4(d), with f_1 and f_2 clearly marked. As noted, the electric field at $f_1 = 985$ MHz is higher than at $f_2 = 3$ GHz, indicating potentially better sensitivity at f_1 . However, in this first



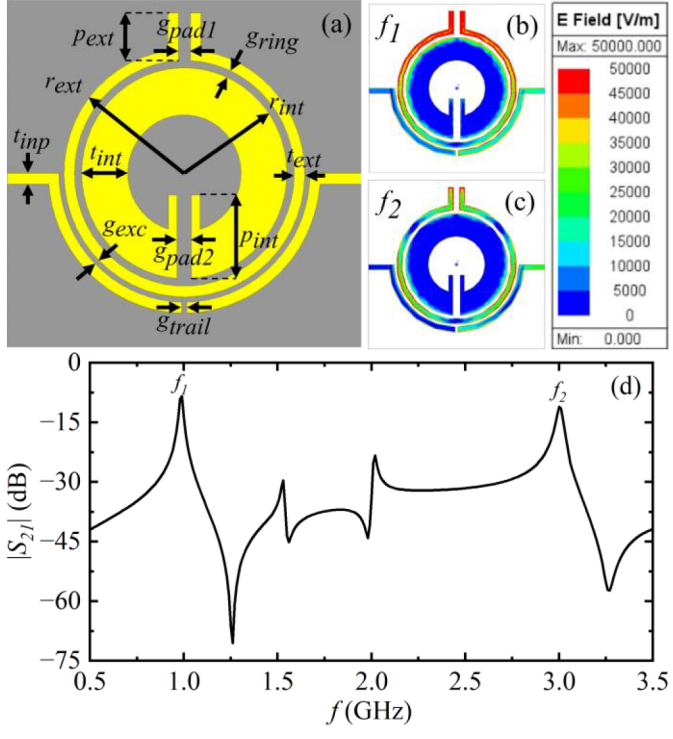


Fig. 4. DCCSRR final geometry and its simulation frequency response. In (a), the DCCSRR final geometry is considered, in (b) and (c), the electric fields at two resonance peaks, at $f_1 = 985$ MHz and $f_2 = 3$ GHz, are shown, while in (d), its frequency response in magnitude is presented.

TABLE I
DCCSRR GEOMETRIC PARAMETERS IN (mm)

Parameter	r_{ext}	r_{int}	g_{pad1}	g_{pad2}	t_{inp}	g_{ring}
Dimension	17.00	14.50	1.70	1.70	1.50	1.00
Parameter	p_{int}	p_{ext}	g_{trail}	g_{exc}	t_{ext}	t_{int}
Dimension	11.47	6.52	0.70	0.70	1.50	6.50

resonance region, the losses for ABPS are higher, as shown in Fig. 3(b), which would significantly compromise the resonance amplitude and, consequently, the SNR. However, further experimental data are required to confirm these observations, and this will be analyzed subsequently.

To adapt the structure for glucose sensing, a sample container was strategically positioned over the region with the highest electric field intensity, as shown in Fig. 4(b) and (c). Fig. 5(a) presents this setup in an isometric view, where the container is illustrated in orange, with a sample represented in green. Fig. 5(b) provides a side view, showing only the essential components, while Fig. 5(c) shows a front view, detailing the sample container and its dimensions. In addition, a 150- μ m-thick glass disk layer (matching the container diameter) was added to the bottom of the container to secure the samples. Glass was selected due to its low-loss characteristics, and this thin layer enhances sample interaction, thereby increasing sensitivity.

The optimized DCCSRR was fabricated using electronic prototyping, specifically with an LPKF machine, model S-103. Silver nitrate (AgNO₃) was deposited on the copper traces

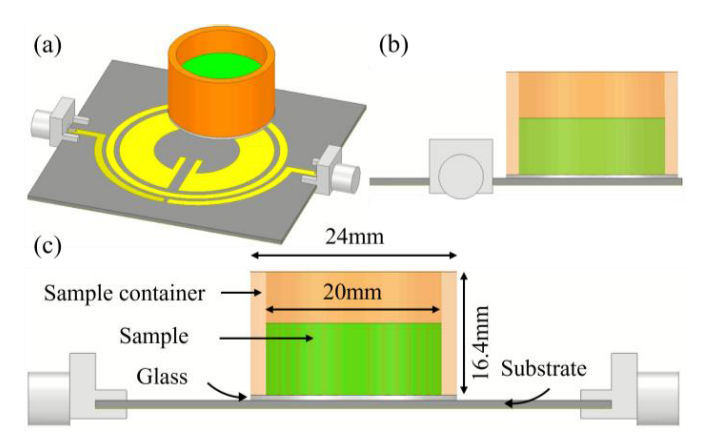


Fig. 5. Representation of the 3-D schematic of the DCCSRR and sample container, which was fabricated using a resin 3-D printer and positioned in the region of highest electric field. The bottom of the container is covered with a thin glass disk layer to enhance interaction (and thereby improving sensitivity) while preventing the liquid from directly contacting the sensor. (a) Isometric view, (b) lateral view, and (c) frontal view, detailing the container's dimensions. The green color represents a given sample.

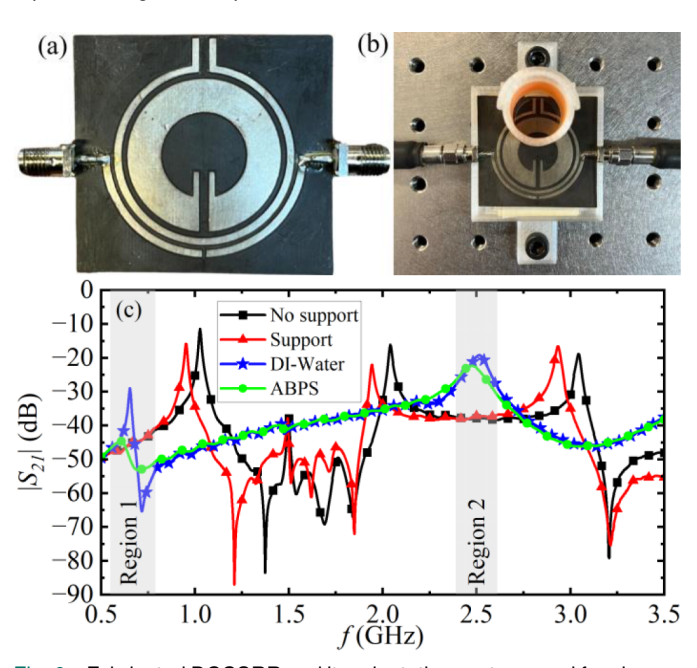


Fig. 6. Fabricated DCCSRR and its adaptation system used for glucose sensing. In (a), fabricated DCCSRR is shown; in (b), DCCSRR is inserted into the adaptation system; and in (c), $|S_{21}|$ curves: without support (black lines), with the supports added (red lines), with DI-water in the sample holder (blue lines), and with ABPS in the sample holder (green lines).

to prevent oxidation over time. The connectorized sensor is depicted in Fig. 6(a), while in Fig. 6(b), it is positioned within an ABS plastic support (white component) to ensure stability. The DCCSRR was tested in the VNA under four different conditions: without any support, with the supports added, and with DI-water and ABPS in the reservoir. Fig. 6(c) presents the results for the same frequency range as the simulated results. The black line represents the experimental sensor response without any sample in the reservoir, showing good agreement with the simulation results depicted in Fig. 4(d). The red line highlights the effect of the supports, showing a redshift compared to the black line. The blue and green lines

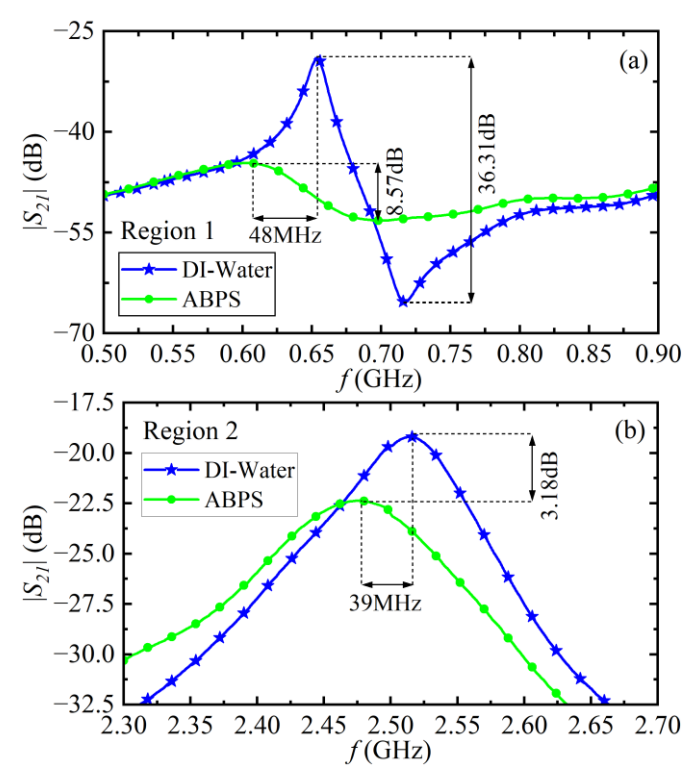


Fig. 7. Experimental transmission coefficients obtained from DCCSRR when pure DI-water (blue lines) and ABPS (green lines) are considered. In (a), comparison is done in the Region 1, which clearly shows how different the sensor's response is when these two liquids are tested. In (b), same comparison is repeated, but in Region 2, which presents minor changes for the tested samples.

indicate the responses when DI-water and ABPS, respectively, are added to the reservoir.

As observed, the liquids significantly attenuate the DCC-SRR response due to their inherent losses, resulting in only two resonances appearing within the band, highlighted by Regions 1 and 2. To determine the volume, initially, a sample of 1 mL was tested, but due to the large surface area of the sample holder (required to cover the high electric field region), the liquid was not evenly distributed at the bottom, leading to unstable measurements. To resolve this issue, the sample volume was doubled to 2 mL, which effectively eliminated the instability.

Fig. 7(a) focuses on Region 1, clearly reaffirming the earlier discussion: at low frequencies, ABPS (green lines) exhibits much higher absorption than DI-water (blue lines), resulting in an attenuation exceeding 27 dB relative to the DI-water response and cause a resonance shift of nearly 50 MHz. Although ABPS is more representative than DI water, it makes it difficult for the DCCSRR to detect small amplitude variations at 650 MHz due to its pronounced impact on the resonance as earlier mentioned. It is important to emphasize that similar signal degradation would be observed if any MW resonator were to switch its reference sample from DI-water to ABPS at low frequencies. Such a substitution would also shift the operating point, rendering the sensor ineffective at its originally intended frequency.

Fig. 7(b) presents Region 2, the second resonance observed in Fig. 6(c) for DI-water (blue line) and ABPS (green line).

The displacement observed for ABPS compared to DI-water is approximately 40 MHz, consistent with the permittivity data shown in Fig. 3(a). Similarly, the amplitude difference observed in Region 2 is around 3 dB, which aligns with the findings in Fig. 3(b), as the losses of these two samples are closer in Region 2 than in Region 1. Based on the previous discussion, we conclude that the DCCSRR achieves optimal performance when operated in Region 2 at 2.48 GHz, defining this as its operating point.

Section IV presents the DCCSRR's response to DI water and ABPS at different glucose concentrations, its performance under repeated measurements, a comparison with other alternatives, and a final discussion of its limitations and future perspectives.

IV. EXPERIMENTAL RESULTS

A. DCCSRR Performance

After determining the operating point, the next step is to analyze the DCCSRR sensitivity to various glucose concentration levels. The samples are prepared using DI-water and ABPS. The following concentrations are considered: 400, 350, 300, 250, 200, 150, 100, 50, 25, and 0 mg/dL. As previously mentioned, the relevant range for glucose monitoring in diabetes patients is from 50 to 300 mg/dL [32]. The selected solutions extend beyond this range to ensure that the DCCSRR operates effectively even under critical conditions. Moreover, the concentration set provides two types of variations, 50 and 25 mg/dL, to test the DCCSRR's sensitivity. The glucose samples were weighed using an i-ThermoGA64M (Bel Engineering) scale, and all measurements were conducted at 25 °C \pm 0.5 °C in a controlled indoor environment. Fig. 8 shows the fit curves obtained experimentally from the VNA for the previous situation, but they can be visualized in their original form in Fig. S2.

Fig. 8(a) shows the fit magnitude of the transmission coefficient based on experimental data, $|S_{21}^{\text{DI-water}}(C)|$, for DI-water, where C refers to the glucose concentration level in mg/dL. The curves are well-organized with a decrease of the resonance amplitude and a redshift of the frequency as C decreases. This behavior is consistent with the permittivity curves for glucose diluted in DI-water [49], since curves with lower glucose levels exhibit higher permittivity and lower losses compared to those with higher concentrations, resulting in a redshift for lower concentrations. Fig. 8(b) represents the fit values for $|S_{21}^{ABPS}(C)|$ considering the same set of concentrations, but with DI-water replaced by ABPS. The dotted gray lines represent the optimal performance point of the sensor when measurements are repeated, but they will be thoroughly analyzed later. Note that the resonances with ABPS exhibit a more pronounced attenuation compared to DI-water, along with a lower quality factor. This is attributed to the additional losses inherent to ABPS. Furthermore, the attenuation levels show proportional losses as the concentration changes, aligning with the imaginary part of the ABPS complex permittivity curves in Fig. 3(b).

Note that the reference change between DI-water and ABPS measurements leads to different frequency shifts and attenuation levels across all concentrations. Although this

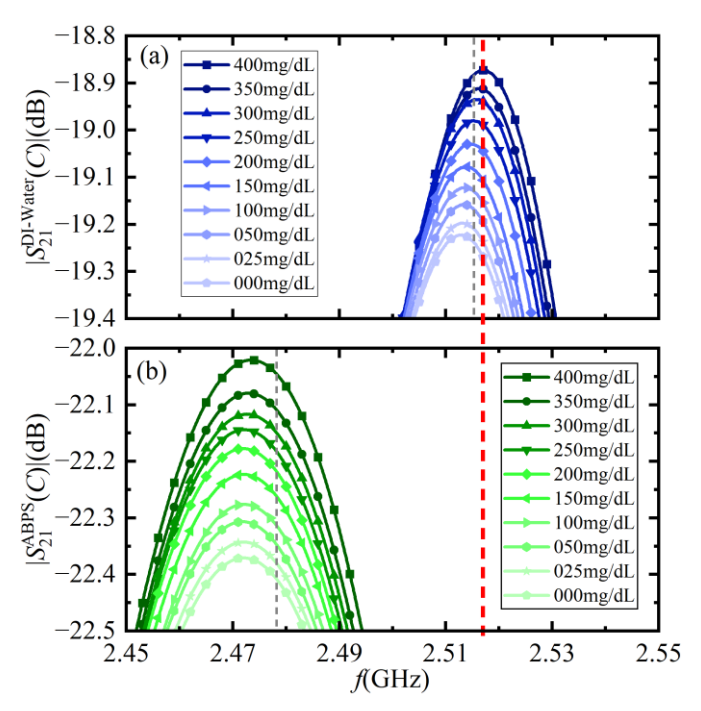


Fig. 8. Fit experimental $|S_{21}(C)|$ for the DCCSRR tested with DI-water solution with glucose added in (a) and ABPS with glucose added in (b), considering the same mode found at 3 GHz and with concentrations ranging from 0 to 400 mg/dL. The dashed gray lines refer to the DCCSRR's operation point. Original experimental dataset are available in Fig. S2 of the supplemental material.

modification may appear minor, a sensor designed to operate at the DI-water resonance peak would, when utilized with ABPS, function at a point red-shifted with respect to the ABPS resonance peak, at a position determined by the red line in Fig. 8(b). This offset point would be substantially distant from the ABPS resonance peak. In this region, the amplitude differences between concentrations are considerably reduced when compared to those at the resonance peak. While these differences might still appear distinguishable, the inherent background noise in the measurement process degrades the sensor accuracy, making it less sensitive to detecting low concentrations. This is clearly illustrated in Fig. S2, where a specific ABPS measurement set is considered. At a frequency point midway through the actual shift between the ABPS and DI-water resonances, the curves for lower concentrations tend to overlap, as the SNR worsens in this region. This highlights the crucial role SNR plays in our design requirements.

To evaluate the DCCSRR's performance, three measurements were repeated for each concentration level using both DI-water and ABPS. Fig. 9(a) illustrates the sensor's performance for DI-water at 2.515 GHz [gray line in Fig. 8(a)]. Symbols correspond to the experimental measurements, while error bars indicate the standard deviation for each concentration. As shown, the error bars do not overlap, demonstrating the DCCSRR's capability to detect variations of 25 mg/dL. A second-order polynomial was used to fit the data, represented by the dashed lines, which achieved an *R*-squared value of 0.998, indicating strong agreement with the experimental data. The fitting curve is expressed as

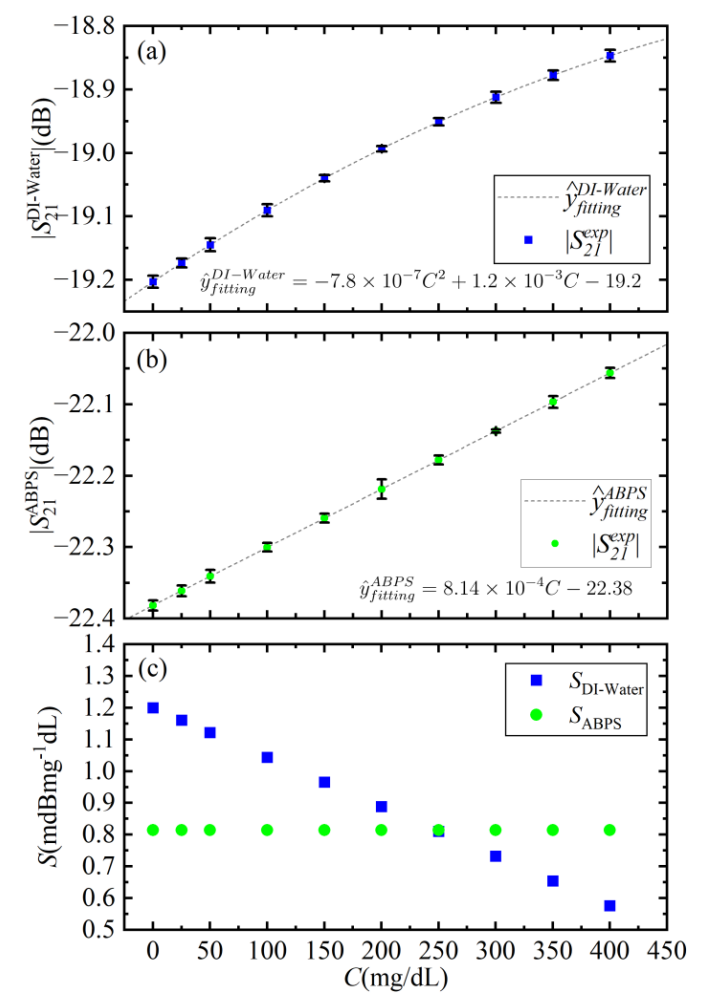


Fig. 9. Repeated experimental measurements for the DCCSRR when, in (a), operating frequency is 2.477 GHz and DI-water is used as the reference. In (b), operating frequency is 2.515 GHz and ABPS is used as the reference. In (c), sensitivity is calculated for each concentration, considering the two media.

follows:

$$\hat{y}_{2.515\,\text{GHz}}^{\text{DI-water}} = 7.8 \times 10^{-7} C^2 + 1.21 \times 10^{-3} C - 19.203.$$
 (4)

In the second part of the experiment, the DCCSRR was subjected to the same process, using the same concentration levels, but at 2.477 GHz and with ABPS as the reference sample. The results are shown in Fig. 9(b), where the trend is described by the linear function in (5), also with an *R*-squared value of 0.998, signifying a strong correlation between the experimental data and the fit curve

$$\hat{y}_{2.477\,\text{GHz}}^{\text{ABPS}}(C) = 8.04 \times 10^{-4} C - 22.379.$$
 (5)

At the operating frequency, ABPS causes a decrease of approximately 3 dB in $|S_{21}|$ and compromises the quality factor.

Sensitivity is another crucial parameter for estimating the sensor's response to the analyte. Sensitivity can be expressed by calculating the first derivative of (5) at specific concentration points. The results are plotted in Fig. 9(c) for both DI-water and ABPS. As shown, the DCCSRR's sensitivity varies with concentration when DI-water is used as

the reference, while it remains constant for ABPS, evidencing that the sample composition influences the DCCSRR behavior.

Another common metric for assessing sensor reliability is the Clarke error grid analysis (EGA) [51]. This diagram is used to quantify the accuracy of sensors to measure glucose concentration in blood. The x-axis represents the reference concentration ($C_{\rm ref}$), while the y-axis represents the measured values ($C_{\rm meas}$), both in mg/dL. The diagram is divided into five zones: A, B, C, D, and E. Zone A includes variations up to 20% of the reference values and is the most desirable region for sensing. Sensors operating in Zone B have measurement errors greater than 20%, which could lead to incorrect insulin dosages being administered to patients. However, the errors presented by Zone B sensors do not pose a direct risk to the patient's life. Conversely, sensors operating in Zones C, D, and E are unsuitable, as they can endanger the patient's life.

In this context, the Clarke diagram is constructed for the DCCSRR, using (5) and (6) to establish the relationship between the measured variables and the reference concentrations. Fig. 10(a) and (b) shows the results for DI-water and ABPS, respectively. As observed, all data points fall within Zone A, confirming the performance of the proposed sensor. So far, the DCCSRR has been analyzed independently, without any comparison to other technologies; we compare its performance with other existing sensors in the next section.

B. DCCSRR and the Stateof-Art

Table II summarizes the DCCSRR's performance in comparison to other biosensors recently reported in the literature. The DCCSRR operates at 2.48 GHz, an ISM frequency that offers the advantage of cheaper electronic components compared to other alternatives that operate at higher frequencies, such as those in [7], [9], and [11].

Regarding sensing parameters, the DCCSRR operates using the transmission coefficient rather than reflection. This is another advantage, as fewer components are needed for transmission-based measurements. Reflection-based systems require a circulator, which increases the cost and complexity at the commercial stage. A limited number of sensors possess the capability to passively provide frequency shifting at low frequencies, as sensitivity generally diminishes with decreasing frequency. Therefore, the focus is on the transmission coefficient amplitude, which is simpler and more cost-effective.

In terms of signal levels, at the operating frequency, our DCCSRR sensor provides signals around -19 dB (~ 35 mVp) for DI-water and -22 dB (~ 25 mVp) for ABPS, considering an input power of 0 dBm and a line impedance of 50 Ω . These values are significant as they fall within an acceptable range to be measured by typical microcontrollers. Conversely, signals that are excessively low, as reported in [9], [11], [22], [23], and [24], can be read by a VNA but will require costly amplifiers and analog-to-digital converters to be precisely measured, making the sensor less attractive at a commercial stage. For instance, a sensor that

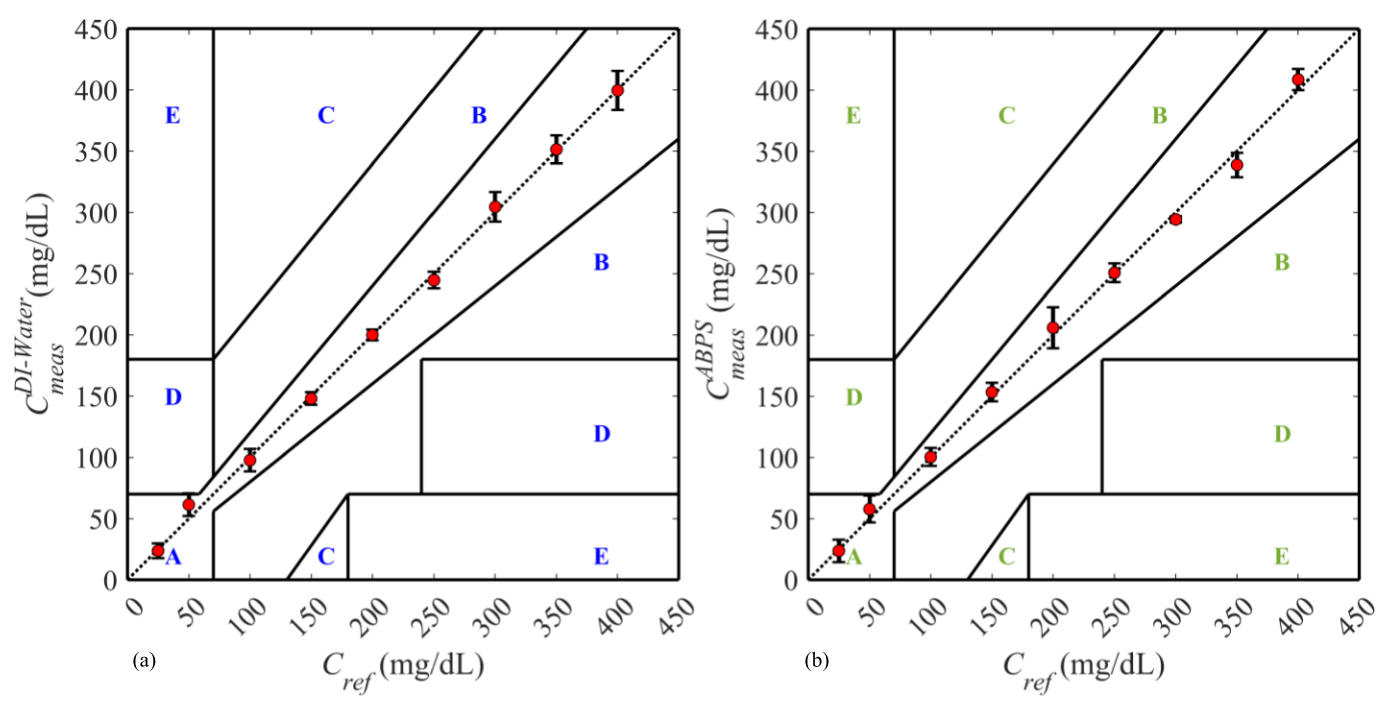


Fig. 10. Resulting Clarke error grids for the DCCSRR when operated using (a) DI-water and (b) ABPS as reference samples for the following concentrations: 25, 50, 100, 150, 200, 250, 300, 350, and 400 mg/dL.

TABLE II

COMPARISON OF RECENTLY PUBLISHED GLUCOSE SENSORS IN THE MW BAND USING ML TECHNOLOGY

Reference	Frequency (GHZ)	Sensing Parameter	Signal Levels (dB)	Minimal measured concentration (mg/dL)	Measured Range (mg/dL)	Passive Sensor	Non- Licensed band	Sensitivity per (mg/dL)	Size (mm²)	Year
[7]	6.07	$ \Delta S_{2I} $	-32.0	50	0-250	Yes	Yes	19mdB	(20.4×40.4)	2019
[8]	2.42	$ \Delta S_{2I} $	-16.8	100	0-400	No	No	10mdB	N.A.	2020
[9]	5.15	$ \Delta S_{2I} $, Δf_r	-65.0	100	100-300	Yes	No	320KHz	(70×40)	2021
[10]	1.8, 1.9	$ \Delta S_{II} $	-10.8	50	0-250	No	No	0.4mdB	(56×30.6)	2021
[15]	2.26	$ \Delta S_{2I} $	-50.0	50	0-400	No	No	13mdB	N.A.	2021
[11]	12.9,16.4	Δf_r	-55.0	100	100-800	Yes	No	143KHz	(125×42)	2022
[28]*	3.02	$ \Delta S_{2I} $	11.2	50	50-400	No	No	2mdB	N.A.	2022
[29]*	3.24	$ \Delta S_{II} $	-18	25	0-500	No	No	8.5mdB	N.A.	2023
[12]	2.32	$ \Delta S_{2I} $, $ \Delta S_{II} $	-12.5	30	89-456	Yes	No	950KHz	N.A.	2023
[13]	1.9, 4.46	$ \Delta S_{II} $, Δf_r	-52.0	200	0-1800	Yes	No	10KHz	(22×12)	2023
[14]	1.47,3.43	$ \Delta S_{21} $, Δf_r	- 96	100	0-800	No	No	99KHz	(100×35)	2024
This Work**	2.48	$ \Delta S_{2I} $	-22.2	25	0-400	Yes	Yes	0.81mdB	(49×45)	2024

*Interstitial fluid used as reference sample; **Artificial blood plasma solution used as reference sample; N/A refers to unavailable data.

operates at -55 dB would have its mean values around 0.56 mVp, without considering concentration steps that would be even smaller. This underscores the importance of the SNR discussion.

The DCCSRR also offers other advantages over existing technologies, such as its ability to detect glucose variations as small as 25 mg/dL, a precision superior to all other analyzed sensors [16], [17], [18], [19], [20], [21], [22], [23], [24]. In addition, its measuring range of 0–400 mg/dL fully covers the relevant range for diabetes patients (50–300 mg/dL), which is not addressed by Odabashyan et al. [7], Hanna et al. [18], Moloudian et al. [19], Basit et al. [20], and Gao et al. [21]. Its passive nature ensures simpler operation compared to active platforms [8], [10], [14], [15]. Moreover, its measuring capabilities within the unlicensed ISM band offer advantages over others [17], [18], [19], [20], [21], [22], [23], [24].

Note that among the compared sensors, both frequency shift and amplitude approaches are present. Given that frequency and amplitude are distinct quantities, it is important to emphasize that the sensitivity values are reported in mdB per (mg/dL) or in kHz per (mg/dL), depending on the approach utilized by each specific reference. In addition, although the DCCSRR exhibits a relatively low sensitivity value per (mg/dL), its measurements demonstrate high stability and minimal deviation for the same glucose concentration, enabling the sensor to detect glucose concentrations in ABPS as low as 25 mg/dL, which is the lowest value alongside [29]. Moreover, the DCCSRR possesses comparable dimensions relative to the other sensors. Lastly, the DCCSRR can measure glucose variations from 0 to 400 mg/dL using ABPS, which better mimics BP rather than DI-water. This capability is not assured by all other MW resonators [16], [17], [18], [19], [20], [21], [22], [23], [24].

Although the DCCSRR has demonstrated strong performance, it shares a common limitation with MW sensors for water-based samples: the need for temperature stability, which can compromise measurements. A potential solution is to adapt a differential design to the DCCSRR, as seen in [8], enabling differential measurements that mitigate temperature variations and increase robustness.

The use of plasma samples is also a drawback, as it requires an invasive procedure for collection and analysis. However, since the DCCSRR was designed as a flexible platform with potential for future enhancements, noninvasive measurements are certainly a consideration. Its resonances fall within a favorable frequency range (<3 GHz), enabling electromagnetic fields to penetrate and reach glucose concentrations in blood vessels [52]. This capability, combined with the use of amplifiers, could significantly enhance the sensor's sensitivity and accuracy, paving the way for fully noninvasive measurements.

Scalability is not a significant concern, as PCB prototyping machines can produce large numbers of structures with high reproducibility and low cost. In addition, the DCCSRR benefits from low power consumption, requiring only 0 dBm, and readings are completed in just a few seconds, making battery life a minor concern. Considering these factors, the DCCSRR offers a wide range of potential applications, extending its capabilities and supporting new innovations.

V. CONCLUSION

In this article, we present two major contributions to the MW sensing field. The first one reveals that DI-water, the most used reference sample to represent BP in MW sensing, has electromagnetic properties that are significantly different when compared to BP. These differences are more pronounced when losses are considered, especially in the range from 0.5 up to 3 GHz. The reference sample used for comparison was the ABPS, a laboratory-synthesized solution that closely resembles real BP. When the complex permittivity of DI-water and ABPS are compared, they present significant differences, showing that DI-water is not as accurate a representation of BP as ABPS. This occurs due to the ion effect, which is not observable in DI-water.

In the second approach, we propose the DCCSRR, a structure designed and fabricated to operate in the ISM band, specifically at 2.48 GHz. The DCCSRR was assessed when DI-water and ABPS were tested under different glucose levels (0, 25, 50, 100, 150, 200, 250, 300, 350, and 400 mg/dL), showing different behaviors for DI-water and ABPS, and therefore, aligning with the first analysis. Furthermore, the DCCSRR achieved a remarkable result, as it was able to detect variations as small as 25 mg/dL for both DI-water and ABPS, passively. In addition, when the DCCSRR measurements were analyzed using the Clarke diagram, they remained in the A category, with low dispersion among concentrations. All these achievements together demonstrate the potential of the DCCSRR as a promising, sensitive, and low-cost alternative for the MW sensors field.

REFERENCES

- [1] International Diabetes Federation, Brussels, Belgium. (2021). *IDF Diabetes Atlas*. [Online]. Available: https://www.diabetesatlas.org
- [2] K. L. Ong et al., "Global, regional, and national burden of diabetes from 1990 to 2021, with projections of prevalence to 2050: A systematic analysis for the global burden of disease study 2021," *Lancet*, vol. 402, no. 10397, pp. 203–234, Jun. 2023.
- [3] A. E. Omer et al., "Low-cost portable microwave sensor for non-invasive monitoring of blood glucose level: Novel design utilizing a four-cell CSRR hexagonal configuration," Sci. Rep., vol. 10, no. 1, p. 15200, Sep. 2020.
- [4] M. C. Cebedio, L. A. Rabioglio, I. E. Gelosi, R. A. Ribas, A. J. Uriz, and J. C. Moreira, "Analysis and design of a microwave coplanar sensor for non-invasive blood glucose measurements," *IEEE Sensors J.*, vol. 20, no. 18, pp. 10572–10581, Sep. 2020.
- [5] C. Srichan, W. Srichan, P. Danvirutai, C. Ritsongmuang, A. Sharma, and S. Anutrakulchai, "Non-invasively accuracy enhanced blood glucose sensor using shallow dense neural networks with NIR monitoring and medical features," *Sci. Rep.*, vol. 12, no. 1, p. 1769, Feb. 2022.
- [6] M. I. O. Souza, A. F. D. Mota, V. M. Pepino, J. P. Carmo, and B. V. Borges, "Multi-purpose microwave biosensor based on signal encoding technique and microfluidics for improved sensitivity," *IEEE Sensors J.*, vol. 21, no. 4, pp. 4571–4581, Feb. 2021.
- [7] L. Odabashyan et al., "Real-time noninvasive measurement of glucose concentration using a modified Hilbert shaped microwave sensor," *Sensors*, vol. 19, no. 24, p. 5525, Dec. 2019.
- [8] C. Jang, J.-K. Park, H.-J. Lee, G.-H. Yun, and J.-G. Yook, "Non-invasive fluidic glucose detection based on dual microwave complementary split ring resonators with a switching circuit for environmental effect elimination," *IEEE Sensors J.*, vol. 20, no. 15, pp. 8520–8527, Aug. 2020.
- [9] A. A. Shahri, A. H. Omidvar, G. P. Rehder, and A. L. C. Serrano, "A high sensitivity microwave glucose sensor," *Meas. Sci. Technol.*, vol. 32, no. 7, Jul. 2021, Art. no. 075104.
- [10] M. A. Zidane, A. Rouane, C. Hamouda, and H. Amar, "Hyper-sensitive microwave sensor based on split ring resonator (SRR) for glucose measurement in water," Sens. Actuators A, Phys., vol. 321, Apr. 2021, Art. no. 112601.
- [11] A. Kandwal et al., "Young's double slit method-based higher order mode surface plasmon microwave antenna sensor: Modeling, measurements, and application," *IEEE Trans. Instrum. Meas.*, vol. 71, pp. 1–11, 2022.
- [12] P. Mohammadi, A. Mohammadi, and A. Kara, "Dual-frequency microwave resonator for noninvasive detection of aqueous glucose," *IEEE Sensors J.*, vol. 23, no. 18, pp. 21246–21253, Sep. 2023.
- [13] Z. Yi and C. Wang, "Noninvasive glucose sensors using defective-ground-structure coplanar waveguide," *IEEE Sensors J.*, vol. 23, no. 1, pp. 195–201, Jan. 2023.
- [14] S. Wang, W. Wang, and Y. Zheng, "Reconfigurable multimode microwave sensor with resonance and transmission sensing capabilities for noninvasive glucose monitoring," *IEEE Trans. Microw. Theory Techn.*, vol. 72, no. 5, pp. 3102–3117, May 2024.
- [15] C. Jang, J.-K. Park, H.-J. Lee, G.-H. Yun, and J.-G. Yook, "Sensitivity-enhanced fluidic glucose sensor based on a microwave resonator coupled with an interferometric system for noninvasive and continuous detection," *IEEE Trans. Biomed. Circuits Syst.*, vol. 15, no. 5, pp. 1017–1026, Oct. 2021.
- [16] H.-T. Zhu et al., "Low-cost narrowed dielectric microstrip line—A three-layer dielectric waveguide using PCB technology for millimeter-wave applications," *IEEE Trans. Microw. Theory Techn.*, vol. 65, no. 1, pp. 119–127, Jan. 2017.
- [17] A. Kandwal, L. W. Liu, M. J. Deen, R. Jasrotia, B. K. Kanaujia, and Z. Nie, "Electromagnetic wave sensors for noninvasive blood glucose monitoring: Review and recent developments," *IEEE Trans. Instrum. Meas.*, vol. 72, pp. 1–15, 2023.
- [18] J. Hanna et al., "Wearable flexible body matched electromagnetic sensors for personalized non-invasive glucose monitoring," Sci. Rep., vol. 12, no. 1, p. 14885, Sep. 2022.
- [19] G. Moloudian, S. Bahrami, and R. M. Hashmi, "A microstrip low-pass filter with wide tuning range and sharp roll-off response," *IEEE Trans. Circuits Syst. II, Exp. Briefs*, vol. 67, no. 12, pp. 2953–2957, Dec. 2020.

- [20] A. Basit, M. I. Khattak, A. R. Sebak, A. B. Qazi, and A. A. Telba, "Design of a compact microstrip triple independently controlled pass bands filter for GSM, GPS and WiFi applications," *IEEE Access*, vol. 8, pp. 77156–77163, 2020.
- [21] D. Gao, Z.-X. Cao, S.-D. Fu, X. Quan, and P. Chen, "A novel slot-array defected ground structure for decoupling microstrip antenna array," *IEEE Trans. Antennas Propag.*, vol. 68, no. 10, pp. 7027–7038, Oct. 2020.
- [22] Y. Jia, Y. Liu, and Y. Zhang, "A 24 GHz microstrip antenna array with large space and narrow beamwidth," *Microw. Opt. Technol. Lett.*, vol. 62, no. 4, pp. 1615–1620, Apr. 2020.
- [23] S. Hosseinzadeh and M. Yousefi, "A permittivity and conductivity sensor based on microstrip transmission line with defective ground for detection of urea in saline," *IEEE Trans. Instrum. Meas.*, vol. 73, pp. 1–11, 2024.
- [24] M. Alibakhshikenari et al., "A comprehensive survey on antennas on-chip based on metamaterial, metasurface, and substrate integrated waveguide principles for millimeter-waves and terahertz integrated circuits and systems," *IEEE Access*, vol. 10, pp. 3668–3692, 2022
- [25] N. Hussain, M.-J. Jeong, A. Abbas, T.-J. Kim, and N. Kim, "A metasurface-based low-profile wideband circularly polarized patch antenna for 5G millimeter-wave systems," *IEEE Access*, vol. 8, pp. 22127–22135, 2020.
- [26] A. Javed, A. Arif, M. Zubair, M. Q. Mehmood, and K. Riaz, "A low-cost multiple complementary split-ring resonator-based microwave sensor for contactless dielectric characterization of liquids," *IEEE Sensors J.*, vol. 20, no. 19, pp. 11326–11334, Oct. 2020.
- [27] H.-Y. Gan et al., "Differential microwave microfluidic sensor based on microstrip complementary split-ring resonator (MCSRR) structure," *IEEE Sensors J.*, vol. 20, no. 11, pp. 5876–5884, Jun. 2020.
- [28] N. Kazemi and P. Musilek, "Enhancing microwave sensor performance with ultrahigh Q features using CycleGAN," IEEE Trans. Microw. Theory Techn., vol. 70, no. 12, pp. 5369–5382, Dec. 2022.
- [29] N. Kazemi, M. Abdolrazzaghi, P. E. Light, and P. Musilek, "In-human testing of a non-invasive continuous low-energy microwave glucose sensor with advanced machine learning capabilities," *Biosensors Bioelectron.*, vol. 241, Dec. 2023, Art. no. 115668.
- [30] A.-M. Brady, C. McCabe, and M. McCann, Fundamentals of Medical-Surgical Nursing: A Systems Approach. Hoboken, NJ, USA: Wiley, 2014.
- [31] A. Oyane, H. Kim, T. Furuya, T. Kokubo, T. Miyazaki, and T. Nakamura, "Preparation and assessment of revised simulated body fluids," J. Biomed. Mater. Res. A, Soc. Biomater., Jpn. Soc. Biomater., Austral. Soc. Biomater. Korean Soc. Biomater., vol. 65A, no. 2, pp. 188–195, May 2003.
- [32] M. A. Pleitez, T. Lieblein, A. Bauer, O. Hertzberg, H. Von Lilienfeld-Toal, and W. Mäntele, "In vivo noninvasive monitoring of glucose concentration in human epidermis by midinfrared pulsed photoacoustic spectroscopy," *Anal. Chem.*, vol. 85, no. 2, pp. 1013–1020, Jan. 2013.
- [33] J. Z. Bao, C. C. Davis, and M. L. Swicord, "Microwave dielectric measurements of erythrocyte suspensions," *Biophys. J.*, vol. 66, no. 6, pp. 2173–2180, Jun. 1994.
- [34] K. You, H. Mun, L. You, J. Salleh, and Z. Abbas, "A small and slim coaxial probe for single Rice grain moisture sensing," *Sensors*, vol. 13, no. 3, pp. 3652–3663, Mar. 2013.
- [35] T. Meissner and F. J. Wentz, "The complex dielectric constant of pure and sea water from microwave satellite observations," *IEEE Trans. Geosci. Remote Sens.*, vol. 42, no. 9, pp. 1836–1849, Sep. 2004.
- [36] Y. Z. Cheng, H. L. Yang, Y. Nie, R. Z. Gong, and Z. Z. Cheng, "Investigation of negative index properties of planar metamaterials based on split-ring pairs," *Appl. Phys. A, Solids Surf.*, vol. 103, no. 4, pp. 989–994, Jun. 2011.
- [37] M. Moniruzzaman, M. T. Islam, M. R. Islam, N. Misran, and M. Samsuzzaman, "Coupled ring split ring resonator (CR-SRR) based epsilon negative metamaterial for multiband wireless communications with high effective medium ratio," *Results Phys.*, vol. 18, Sep. 2020, Art. no. 103248.
- [38] M. Rashedul Islam et al., "Square enclosed circle split ring resonator enabled epsilon negative (ENG) near zero index (NZI) metamaterial for gain enhancement of multiband satellite and radar antenna applications," *Results Phys.*, vol. 19, Dec. 2020, Art. no. 103556.

- [39] H. J. El-Khozondar, M. Abu-Marasa, R. J. El-Khozondar, M. Elbahri, and S. Zouhdi, "Design of voltage control oscillator using nonlinear composite right/left-handed transmission line," Adv. Electromagn., vol. 5, no. 1, p. 15, Mar. 2016.
- [40] M. O. M. Abu-Marasa and H. J. El-Khozondar, "A compact very wide-band amplifying filter based on RTD loaded composite right/left-handed transmission lines," *SpringerPlus*, vol. 4, no. 1, pp. 1–6, Dec. 2015.
- [41] D. Huang et al., "A microstrip dual-split-ring antenna array for 5G millimeter-wave dual-band applications," *IEEE Antennas Wireless Propag. Lett.*, vol. 21, no. 10, pp. 2025–2029, Oct. 2022.
- [42] O. Niksan, M. C. Jain, A. Shah, and M. H. Zarifi, "A nonintrusive flow rate sensor based on microwave split-ring resonators and thermal modulation," *IEEE Trans. Microw. Theory Techn.*, vol. 70, no. 3, pp. 1954–1963, Mar. 2022.
- [43] W.-J. Wu and W.-S. Zhao, "A quality factor enhanced microwave sensor based on modified split-ring resonator for microfluidic applications," *IEEE Sensors J.*, vol. 22, no. 23, pp. 22582–22590, Dec. 2022.
- [44] M. Nosrati, F. Soltanian, and A. Nosrati, "Sensitivity enhancement of microwave split-ring-resonator sensors," *IEEE Trans. Compon., Packag., Manuf. Technol.*, vol. 14, no. 5, pp. 921–929, May 2024.
- [45] J. Xie, J. Wen, J. Chen, and W. Yuan, "Microwave icing sensor based on interdigital-complementary split-ring resonator," *IEEE Sensors J.*, vol. 22, no. 13, pp. 12829–12837, Jul. 2022.
- [46] D. Kilani, F. Niknahad, A. Shah, S. Olsen, M. Meaker, and M. H. Zarifi, "Wireless microwave sensor network using split ring resonators for ice monitoring applications," *IEEE Internet Things J.*, vol. 11, no. 14, pp. 25316–25325, Jul. 2024.
- [47] O. Niksan, K. Colegrave, and M. H. Zarifi, "Battery-free, artificial neural network-assisted microwave resonator array for ice detection," *IEEE Trans. Microw. Theory Techn.*, vol. 71, no. 2, pp. 698–709, Feb. 2023.
- [48] Y. Feng, Z. Li, L. Qi, W. Shen, and G. Li, "A compact and miniaturized implantable antenna for ISM band in wireless cardiac pacemaker system," Sci. Rep., vol. 12, no. 1, p. 238, Jan. 2022.
- [49] V. Turgul and I. Kale, "Permittivity extraction of glucose solutions through artificial neural networks and non-invasive microwave glucose sensing," Sens. Actuators A, Phys., vol. 277, pp. 65–72, Jul 2018
- [50] ANSYS, Canonsburg, PA, USA. (Jan. 2024). HFSS: High Frequency Structure Simulator. [Online]. Available: https://www.ansys.com/
- [51] W. L. Clarke, D. Cox, L. A. Gonder-Frederick, W. Carter, and S. L. Pohl, "Evaluating clinical accuracy of systems for self-monitoring of blood glucose," *Diabetes Care*, vol. 10, no. 5, pp. 622–628, Sep. 1987.
- [52] T. Yilmaz, R. Foster, and Y. Hao, "Radio-frequency and microwave techniques for non-invasive measurement of blood glucose levels," *Diagnostics*, vol. 9, no. 1, p. 6, Jan. 2019.

Mateus I. O. Souza was born in Ribeirão Preto, Brazil, in January 1991. He received the B.Sc. degree in electrical engineering from the Universidade Federal do Triângulo Mineiro (UFTM), Uberaba, Brazil, in 2017, and the M.Sc. degree in electrical engineering from São Carlos School of Engineering (EESC), University of São Paulo (USP), São Carlos, Brazil, in 2020, where he is currently pursuing the Ph.D. degree in telecommunications.

His research interests include design of microstrip RF structures, biosensors, signal processing, and machine learning techniques.

Natália M. Santos was born in Rancharia, Brazil, in May 1994. She received the B.Sc. degree from the Faculdade de Ciências e Tecnologia (FCT), Universidade Estadual Paulista (UNESP), Presidente Prudente, Brazil, in 2019, and the M.Sc. degree in physical-chemistry from the Institute of Chemistry of São Carlos (IQSC), University of São Paulo (USP), São Carlos, Brazil, in 2021, where she is currently pursuing the Ph.D. degree in physical-chemistry.

Her research interests include the synthesis of nanomaterials with magnetic and optical properties, modification and functionalization of nanostructures for biomedical applications, and colloidal study of nanomaterials. **Júlio C. P. Alarcon** was born in Ribeirão Preto, Brazil, in June 1998. He received the B.Sc. degree in electrical engineering from Universidade Paulista (UNIP), Ribeirão Preto, in 2020. He is currently pursuing the M.Sc. degree in telecommunications with the University of São Paulo (USP), São Carlos, Brazil.

He is a member of the Metamaterials Group, Microwaves and Optics (GMeta), São Carlos School of Engineering (EESC), USP. His research interests include the simulation, fabrication, and characterization of microwave structures, and machine learning techniques applied to agriculture.

Laudemir C. Varanda received the B.Sc., M.Sc., and Ph.D. degrees in chemistry (physical-chemistry) from the Chemistry Institute of Araraquara, Universidade Estadual Paulista (UNESP), Presidente Prudente, Brazil, in 1996, 1999, and 2003, respectively.

He completed an internship at the Instituto de Ciencia de Materiales de Madrid (ICMM), Madrid, Spain, from 2000 to 2001. He was a Postdoctoral Researcher in Materials Chemistry with UNESP from 2004 to 2006. He has been a Professor with the Chemistry Institute of São Carlos, University of São Paulo (USP), São Carlos, Brazil, since 2007. His current research interests include syntheses, characterization, and self-assembly of nanostructured materials with magnetic, optical, and electronic properties for biomedical, environment, catalysis, sensors, biosensors, and energy applications.

Vinicius M. Pepino received the Ph.D. degree in electrical engineering from the University of São Paulo (USP), São Carlos, Brazil, in 2023.

He is currently a Professor with the Department of Electrical and Computer Engineering (SEL), São Carlos School of Engineering (EESC), USP. His research interests include photonics, microwaves, and metasurfaces, within the Metamaterials Group: Microwaves and Optics (GMeta), USP, with an emphasis on holography, biosensors, and devices for communications.

Ben-Hur V. Borges received the Ph.D. degree in electrical engineering from Drexel University, Philadelphia, PA, USA, in 1997.

From 1997 to 1998, he was a Postdoctoral Researcher with São Carlos School of Engineering (EESC), University of São Paulo (USP), São Carlos, Brazil, where he became an Associate Professor with the Department of Electrical and Computer Engineering (SEL) in 2005. Since 2018, he has been a Full Professor with SEL, EESC, USP. He is the Director of the Metamaterials Group: Microwave and Optics (GMeta), USP. His research interests include metamaterials and metasurfaces for microwave and optical applications, nanoplasmonics, the design and characterization of devices for communications and sensing applications, and the modeling of optical code multiple access networks.

Dr. Borges is an Editorial Board Member of the *Journal of Physics:* Photonics.